Mechanisms of strain accommodation in zircon in a shear zone

Elizaveta Kovaleva*[1,2], Urs Klötzli[2], John Wheeler[3], Gerlinde Habler[2]

[1]Department of Geology, University of the Free State, 205 Nelson Mandela Drive, 9300 Bloemfontein, Free State, South Africa

[2]Department of Lithospheric Research, Faculty of Earth Sciences, Geography and Astronomy, University of Vienna, Althanstrasse 14, A-1090 Vienna, Austria

[3]Department of Earth, Ocean and Ecological Sciences, School of Environmental Sciences, University of Liverpool, L69 3GP, Liverpool, United Kingdom

* Corresponding author.

E-mail: kovalevae@ufs.ac.za

Abstract

Zircon grains with the evidence of crystal-plastic deformation are often found in deformed terrestrial and lunar rocks. In this study we present microstructural data of plastically-deformed zircon crystals that were analyzed in a kinematic context of the respective shear zone. The aims are to describe how orientation of zircon grains in a simple shear affects the zircon deformation mechanisms.

Careful microstructural analyses of zircon crystals in-situ with scanning electron backscatter diffraction (EBSD) mapping show strong geometric relationships between orientations of: (i) the

<c> of plastically-deformed zircon crystals, (ii) the misorientation axes of plastically-deformed zircon crystals and (iii) the XYZ directions of the kinematic framework of a sample. All plastically-deformed zircon crystals have <c> parallel to the XY (foliation plane); crystals with <c> oriented at a higher angle than ca. 15° to the XY plane are undeformed or fractured. Furthermore, zircons that have <c> aligned parallel or normal to X direction (stretching lineation) within the XY plane develop misorientation and rotation axes parallel to [001] and form the <100>{010} slip system and twist boundaries parallel to {001}. Zircons with the <c> aligned at 45□ with respect to X within XY plane can develop two misorientation axes, in ideal case parallel to [001] and [100], and form a combination of tilt and twist low-angle boundaries. These relationships describe the strong geometric control of the macroscopic kinematic rotation axis on the slip systems in zircon, regardless of the grain size and shape. It suggest a tool for constraining an orientation of the plastically deformed zircon with respect to a bulk kinematic rotation axis of the deformation event.

Relationships between zircon deformation mechanisms and macroscopic kinematic frame have important implications for zircon geochronology: if the deformation events result in zircon distortion and rejuvenation of zircon isotopic system, they may be dated. Our microstructural study suggests a criteria for the reliable sample selection for such isotopic dating.

Introduction

Crystal-plastic deformation in zircon has been documented for different geological settings: syn-magmatic deformation (Reddy et al., 2009; Timms and Reddy, 2009), deformation related to ductile shear zones formation (Timms et al., 2006, 2011; Reddy et al., 2006, 2007; Timms and

Reddy, 2009; Flowers et al., 2010; Kaczmarek et al., 2011; Piazolo et al., 2012; MacDonald et al., 2013; Kovaleva et al., 2014), deformation related to the seismic activity (Austrheim and Corfu, 2009; Kovaleva et al., 2015), impact-related lattice distortion (Leroux et al., 1999; Moser et al., 2009, 2011; Nemchin et al., 2009; Timms et al., 2012; Grange et al., 2013). Most often crystal-plastic deformation of zircon is documented in the ductile shear zones and is thus believed to be genetically connected with the deformation event (e.g. Kaczmarek et al., 2011; Piazolo et al., 2012; Kovaleva et al., 2014).

Microstructural analyses of naturally-deformed crystals show that misorientation axes associated with low-angle boundaries have a certain geometric relationship with the macroscopic kinematic rotation axis. Geometric control of the kinematic framework of the shear zone on the activity of crystal slip systems has been described for calcite (Bestmann and Prior, 2002; Reddy and Buchan, 2005), quartz (Menegon et al., 2011) and sillimanite (Piazolo and Jaconelli, 2013). For the simple shear deformation, it has been demonstrated that the rotation axes in plastically-deformed crystals of calcite and sillimanite are parallel to the kinematic rotation axis of the sample (Reddy and Buchan, 2005; Piazolo and Jaconelli, 2013). The assumption that zircon should behave similar to that was inherited by the model of Kaczmarek et al. (2011) describing plastic deformation of zircon in a simple shear framework. However, the misorientation axes of zircons in their sample lie in different orientations and are independent of the deformation framework, which is explained by a post-deformation rigid body rotation of zircon crystals. Thus it was not possible to reconstruct the initial orientation of grains with respect to the kinematic rotation axes, neither to find the corresponding relationships. Kovaleva et al. (2014) have demonstrated crystal-plastically deformed zircon grains with <c> parallel to the stretching lineation and with <100>{010} active slip systems, and suggested that this crystal-plastic deformation mechanism was induced by the specific orientation of the zircons crystals in the shear zone.

In our study we present plastically-deformed zircons from the high-strained rock and confirm that the slip systems geometry is strongly controlled by the orientation of zircon crystals in the simple shear. We describe the zircon deformation evolution in a shear zone, explain its mechanisms, and emphasize the importance of studying crystals in situ, taking into account their orientation to the XYZ framework. Such studies allow to constrain a genetic link of the deformation microstructures in zircon with the deformation event; and have the implications for mineral isotopic geochronology. Plastically-deformed zircon grains could be available for direct dating of the corresponding deformation event.

Sampling locality and sample description

Sampling took place in the Western Tauern Window, Eastern Alps (Zillertal, Tyrol, Austria). In the Tauern Window, continental and oceanic rocks of the Penninic and sub-Penninic nappe sequences are exposed, which represent the footwall of the Austroalpine nappe stack. Nappe stacking and predominant final metamorphism are related to the closure of the Alpine Neotethys and subsequent continental collision in late Cretaceous-Tertiary (Miller et al., 2007). Samples were collected from the “Zillertaler Kern” lobe of the “Zentralgneis” formation (see Selverstone et al., 1991 and reference therein).

The magmatic protholiths of the "Zentralgneis" formation are uppermost Devonian to lower Permian in age. Three magmatic “pulses” of potassium-rich and calc-alkaline granites, felsic and intermediate volcanites and tonalitic/granodioritic plutonites can be distinguished (Veselá et al., 2011). The granitoids intruded into pre-Carboniferous, partly poly-metamorphic basement rocks consisting of various schists, para- and orthogneisses, amphibolites and meta-ophiolites. In the Zillertal section Variscan amphibolite facies regional metamorphism has been overprinted at greenschist- to amphibolite-facies metamorphic conditions of 0.5-0.7 GPa and 550-600° C at ca. 30 Ma and re-equilibrated the rocks (Selverstone, 1991; Pennacchioni and Mancktelow, 2007). Metamorphic (re)crystallization was accompanied by the formation of ductile extensional shear zones that represent a pure strike slip systems (Pennacchioni and Mancktelow, 2007). The sampled shear zone (Fig. 1A) formed during this latter tectono-metamorphic event and the rocks were deformed under greenschist- to amphibolite-facies metamorphism under a simple shear with a minimum of pure shear component.

We have sampled the ~1 m thick ductile shear zone (47°01’18.129"N/11°50’26.709"E), which is exposed on the NE slope of the Zemmbach river side valley and represents strongly foliated quartz-biotite orthogneiss that hosts two adjacent deformed dykes, a leucocratic aplitic dyke and a highly-deformed melanocratic, presumably meta-lamprophyric dyke in the core of the shear zone (Fig. 1A), which was sampled. Analyzed rock contains indicators of the well-developed kinematic framework including foliation, stretching lineation, sigma-clasts and folding of compositional layering (Fig. 1B); the folds axis coincides with the stretching lineation. Foliation plane is used here as the kinematic reference plane (Bestmann and Prior, 2002). The sample is chlorite-rich (>50% modal content) due to intense retrogression of biotite; it is composed of mafic layers consisting of chlorite, biotite and titanite, alternating with the fine-grained plagioclase-quartz layers with an average thickness of 1-6 mm; the compositional layering is isoclinally folded (Fig. 1B). The accessory minerals are calcite, pyrite, zircon, rutile and titanite. Zircon is present as small (10-30 µm) euhedral crystals (Figs. 2, 3) with degraded CL-zonation, with the 1:1 to 1:3 aspect ratio, and are mostly hosted by biotite or chlorite.

Methodology and data representation

Sample preparation

Thin sections were cut at an acute angle of about 45° to the stretching lineation, in order to fully document all relevant deformation microstructures in plastically-deformed zircons. I.e. sample cut parallel to the lineation may not reveal microstructures and subgrain walls that are normal to the kinematic rotation axis of the sample, and thus it would become impossible to document the corresponding geometric relationships. More specific, if we assume that the suggestion given in Kaczmarek et al. (2011) that the rotation axis in the deformed zircon grain is parallel to the kinematic rotation axis of the sample, there should be twist subgrain walls that are by definition normal to the rotation axis. These walls will be not revealed by a classical sample cut normal to the kinematic rotation axis. Therefore, the samples were cut normal to the XY plane but at 45° to the XZ plane.

Zircons were examined in-situ using polished thin sections, mechanically prepared with 0.25 µm diamond paste and subsequently chemically polished with alkaline colloidal silica solution (Köstrosol 3530; pH 9.2-10) on an active rotary head polishing machine for 4 hours.

Electron Backscatter Diffraction (EBSD) analysis and Forescattered electron (FSE) imaging

Zircon crystals were examined for potential crystal-plastic deformation structures using orientation contrast images (Trimby and Prior, 1999; Prior et al., 1999). These were taken using a forescatter-electron detector (FSD) mounted on the EBSD-tube of an FEI Quanta 3D FEG instrument (Center of Earth Sciences, University of Vienna, Austria), which is equipped with a Schottky field emission electron source. Electron beam conditions were 15 kV accelerating voltage, 2.5-4 nA probe current using the analytic mode. Stage settings were at 70° tilt and 14-16 mm working distance. After identification of the potentially deformed crystals, EBSD orientation mapping was applied to selected zircon crystals. The FEI Quanta 3D FEG instrument is equipped with an EDAX Pegasus Apex 4 system consisting of a Digiview IV EBSD camera and an Apollo XV silicon drift detector for EDX analysis. EDX intensities and EBSD data were collected contemporaneously using the OIM data collection software v6.21. An EBSD camera binning of 4x4 was used at exposure times of 50 - 130 milliseconds. As zircon yielded a significantly higher EBSD signal intensity than the matrix phases (used for the background calibration), the EBSD camera exposure time was significantly reduced after background collection in order to avoid signal oversaturation during zircon analysis. Therefore, the matrix phases collected at these settings yielded a very weak pattern contrast. Hough parameters were set to a binned pattern size of 9x9 pixels, a Theta step size of 1° and a Rho-fraction of 74-86%. After applying a 9x9 convolution mask 3 - 15 bands with a minimum pattern contrast of 200 and at a minimum peak distance of 3-10 pixels in Hough space were used for indexing. At the given settings indexing rates were between 6 and 24 points per second. Orientation maps were obtained from the beam scanning in hexagonal grid mode at step sizes of 0.1 – 0.16 micrometer.

The raw indexing for zircon phase shows a very good quality of more than 99.99%. In some cases, after EBSD data collection, the maps were recalculated based on chemical composition of phases with the OIM v6.21 software.

EBSD data representation

The EBSD data are represented in the sample reference frame as false color-coded cumulative misorientation maps, with colors showing the relative angular misorientation of each data point with respect to a user-selected single reference point within the crystal (indicated by a white star marker; Fig. 2). Another mode is so-called “local misorientation” EBSD maps (Fig. 3A), where each pixel is color-coded according to the mean misorientation of the respective data point relative to its neighboring points. The orientations of the crystallographic axes are plotted as lower hemisphere equal area projections and are color-coded according to the corresponding EBSD map (Figs. 2, 3B). Cumulative EBSD maps and pole figures were produced using the EDAX OIM v6.2.1 Analysis software, whereas the local misorientation EBSD maps together with the visualizing of misorientation axis orientation and density contours in the inverse pole figures were generated with the MTEX toolbox for MATLAB (Bachmann et al., 2010, 2011; Mainprice et al., 2011). Presented misorientation axes were calculated with a threshold starting from 1° of misorientation, however for the small misorientations of 1-2° large error is possible (Prior et al., 1999; Reddy and Buchan, 2005; Reddy et al., 2007). By the term “misorientation axis” we imply the crystallographic direction around which two subgrains of the same grain are rotated with respect to each other. By the term “rotation axis” we mean the least dispersed crystallographic axis of the deformed grain in the pole figure, around which all the other grain’s axes are rotating.

Weighed Burgers Vector (WBV) calculations

We also gained insight into geometrically necessary dislocation densities using Weighted Burgers Vector (WBV) calculations (Wheeler et al., 2009; 2012). WBV quantifies the total Burgers vector for all the dislocations passing through the user-selected rectangular region in the EBSD map (the "integral form", according to Wheeler et al., 2009). This can be expressed in terms of lattice vectors and then divided by the sample region area to measure dislocation density including Burgers vector direction. The three numbers, listed for each selected subarea, are the *a*, *b* and *c* components of WBV, measured in $(\mu m)^{-2}$. Rectangular areas with three WBV components were calculated over the EBSD maps with the MATLAB toolbox CrystalScape 1.3 based on the method described in Wheeler et al. (2009, 2012). For this goal the maps were transformed to a rectangular grid and the Euler angles were recalculated accordingly with the Channel software (method described in Kovaleva et al., 2015). However, for the better visual representation, the rectangular areas were superimposed on top of hexagonal "local misorientation" EBSD map.

A non-homogeneous distribution of WBV values in analyzed zircon grain (Fig. 3A) indicates that the plastic deformation in zircon crystal was a post-growth process, and it was caused by directed external differential stress (e.g. MacDonald et al., 2013).

Microstructural and crystallographic zircon data

Zircons in the sample are mostly decoupled from the host matrix, which is indicated by normal and reverse drag of the surrounding biotite and by the open voids parallel to the grains faces (see Kovaleva et al., 2014). Decoupling allows the inhomogeneous distribution of stress within the grains hosted by a rheologically softer material (e.g. see numerical modelling by Schmid and Podladchikov, 2005) and may lead to their crystal-plastic deformation (Kenkmann, 2000; Kovaleva et al., 2014). Microstructural data for the zircons from a sampled meta-lamprophyre demonstrate that some of the grains are crystal-plastically deformed (Figs. 2, 3; see also Kovaleva et al., 2014, Figs. 4, 5 and 9 there); the amount of plastically deformed grains varies from 27 to 38% of all zircon grains in the sample.

Finite deformation pattern of the deformed zircon grains is characterized by the presence of the strain-free subgrains separated by low-angle boundaries and rotated with respect to each other; total misorientation of the subgrains with respect to each other ranges from 3 to 10° (Fig. 2, 3A). Low-angle boundaries traces represent a continues network of step- or zigzag-shaped lines; subgrains represent angular, irregular-shaped domains from 1 to 10 μm in size and with ragged boundaries (Figs. 2, 3A).

Zircons in the analyzed sample generally do not indicate crystallographic preferred orientation and oriented rather randomly (Fig. 4). However, some of the grains that are elongate and sit in the flanks of the compositional folds (e.g. grains 03 and 04, locations marked in Fig. 1B) demonstrate crystallographic preferred orientation. C-axes of those grains are parallel to the fold axes and to the stretching lineation, which may indicate the syn-deformation rigid body rotation of zircon grains in the areas of the highest differential stress (e.g. Jeffery, 1922; Mancktelow et al., 2002). Zircon grains that are not crystal-plastically deformed have <c> at an angle ≥15° to the foliation plane (Fig. 4, open circles). All plastically-deformed crystals from this sample have <c> roughly aligned in the foliation plane (Figs. 2, 3B, 4, solid circles; foliation is subhorizontal).

Crystallographic orientations of <c> of the plastically-deformed zircons 03 and 04 coincide with the orientation of the stretching lineation (Figs. 2A, 3B); grain 15 is oriented with <c> at approximately 45° to the lineation (Fig. 2B); grain 24 has <c> oriented at approximately 90° to the lineation (Fig. 2C).

Presented crystal-plastically deformed zircons have misorientation axes clustering around [001] crystallographic direction (Figs. 2, 3A inset). Grain 15 has additional strong cluster of misorientation axes around [100] (Fig. 2B). Misorientation axes of the grain 24, besides strong clustering around [001], are dispersed in the pole figure forming a few smaller maxima. Grains 03, 24 and 04 reveal rotation of the crystallographic axes around the [001] direction in the pole figures (Figs. 2A-B, 3B). Crystallographic axes in grain 15 are dispersed in a star shape (so-called "asterism" of crystallographic axes, Moser et al., 2009).

Discussion

Analyses of the active slip systems

Presence of the low-angle boundaries gives an opportunity to determine active slip system(s) of dislocations that may be associated with the certain low angle boundary. Low-angle boundaries are the result of crystal recovery, when geometrically necessary dislocations that are formed to accommodate lattice strain assemble together by dislocation creep and form dislocation walls. The geometry of low-angle boundaries, therefore, reflect the slip systems geometry that can be reconstructed (e.g. Reddy et al., 2007; Kaczmarek et al., 2011; Timms et al., 2012). However, we should emphasize that it is not always possible to unequivocally determine what slip system is related to a subgrain boundary, providing only two-dimensional analysis. Therefore, we suggest slip systems that are consistent with a specific boundary.

Grain 03 accommodates a lot of strain by developing a dense network of low-angle boundaries that cause the total misorientation of subgrains of about 10° with respect to each other (Fig. 2A). The traces of low-angle boundaries form zigzag lines with a complicated geometry. We suggest that there are several slip systems operating and changing each other along the low-angle boundaries. All these slip systems have rotation axes around [001] (Fig. 2A, pole figure), which is the most frequent and energetically-preferable rotation axis in zircon (e.g. Leroux et al., 1999; Reddy et al., 2007; Kovaleva et al., 2014). According to their complicated geometry, subgrain boundaries in this grain probably represent both tilt and twist walls (see, for example, analyses of subgrain boundary traces in Reddy et al., 2007).

In grain 15 low-angle boundaries are stretching in two general directions and likely occupy planes (100) and (010) (Fig. 2B, "LAB-1" and "LAB-2" accordingly), and misorientation axes are directed parallel to [001] and <100> crystallographic directions. This imply several possibilities for active slip systems:

a. If the rotation axis for low-angle boundary 1 is [001], then it is a tilt boundary and the slip system should be [100](010).

b. If the rotation axis for low-angle boundary 1 is [100], it's a twist boundary.

c. If the rotation axis for low-angle boundary 1 is [010], it's a tilt boundary with the slip system [100](001).

d. If the rotation axis for the low-angle boundary 2 is [001], it's a tilt boundary with the slip system [010](100).

e. If the rotation axis for the low-angle boundary 2 is [010], it's a twist boundary.

f. If the rotation axis for the low-angle boundary 2 is [100], it's a tilt boundary with the slip system [010](001).

Taking into account that low-angle boundary traces in grain 15 do not follow straight lines and rather represent zigzags, the low-angle boundary network most likely represents a system if interconnected tilt and twist walls with the slip geometries <100>{010} and <100>{001}. Asterism of the crystallographic axes also evidence that there are several slip systems operating at the same time (Moser et al., 2009).

In grain 24 (Fig. 2C) one of the low-angle boundaries ("LAB-1") is parallel to (100) crystallographic plane. Misorientation axis parallel to [001] implies slip system [100]{010} operating in this crystal. The other low-angle boundary, tracing in the lower part of the grain from left to right, has a complicated geometry and most likely represents a result of combination of several slip systems. Minor clusters of misorientation axes around high Miller-indices directions (Fig. 2C) are either a result of analytical error due to low misorientation angles (e.g. Prior, 1999; Reddy and Buchan, 2005); or evidence of minor slips activating to accommodate strain and to connect main tilt and twist walls that have rotation around [001]. The latter is also supported by a minor asterism of crystallographic axes in the pole figure (Fig. 2C).

In grain 04, traces of low-angle boundary 1 (Fig. 3A, "LAB-1") are parallel to (100) plane (Fig. 3B). Misorientation axes in this grain are coinciding with rotation axis and are parallel to [001] (Fig. 3A, inset). Such geometry implies a tilt boundary correlated with the [100]{010} slip system. Low-angle boundary 2 (Fig. 3A, "LAB-2") seems to be parallel to the (110) plane, which implies a tilt boundary with the slip system <-110>{110}. The conclusion is supported by the Weighted Burgers Vector (WBV) calculations (Wheeler et al., 2009, 2012).

WBV is measured in [μm^{-2}] and expressed as three numbers, *a*, *b* and *c*, which are the components of summary Burgers vector across the user-selected selected rectangular area. In the Figure 3A several selected areas with corresponding WBVs values are presented. In the lower left portion of the crystal the WBV values are low (Fig. 3A, gray rectangles), that means that the dislocation density is low and the analyzed domain is strain-free. In the lower right portion WBV is dominated by *a* component (dotted rectangle) which implies dislocations with [100] slip direction (slip system <100>{010}). WBV analysis across low-angle boundary 1 ("LAB-1") shows domination of *b* component (dashed rectangles) that implies dislocations with slip along [010] direction (slip system <010>{100}). WBV analyses across low-angle boundary 2 ("LAB-2") shows high values for *a* and *b* components, implying slip system <-110>{110} with slip along [-110] plane (Fig. 3).

In naturally-deformed crystals it is difficult to find pure edge or screw dislocations. Almost all dislocations have both screw and edge components to them and thus are called mixed dislocations (Poirier, 1985). Mixed dislocations make up most of the dislocations encountered in natural samples and they build networks of low-angle boundaries. To summarize our data, subgrain walls in analyzed zircons appear as zigzag lines that reflects an interplay between tilt dislocations with the slip systems <100>{010} and <-110>{110} and rotation axis [001] and the twist dislocations with the rotation axis [001]. In one case we also observed the possible presence of tilt dislocations with the slip system <100>{001} and rotation axis [010]. In order to accommodate external strain generated in a shear zone, zircon grains develop low-angle boundary network with switching of the glide directions. Rotation axis [001] and slip systems <100>{010} and <100>{001} are the most frequently observed in plastically-deformed zircons (e.g. Leroux, 1999; Reddy et al., 2007; Kovaleva et al., 2014, 2015), and <-110>{110} can be regarded as a newly described slip system (Fig. 3B, “LAB-2”).

Slip along <100>{010} with rotation around [001] is the most energetically preferable geometry of a zircon and is easily activated when zircon has a specific orientation: normal or parallel to the kinematic rotation axis of a shear zone (Figs. 4; 5, cases i and iii). Along the <c> zircon atomic structure consists of chains of alternating edge-sharing SiO_4 tetrahedra and ZrO_8 dodecahedra that are joined laterally by edge-sharing dodecahedra (Robinson et al., 1971; Finch and Hanchar, 2003). In order to develop a slip in the zircon crystal lattice it is easier to break the bonds between SiO_4 tetrahedra and ZrO_8 dodecahedra along <100>, than between the strongly bonded ZrO_8 dodecahedra along [001]. However, if long axis of zircon has a complicated orientation with respect to the kinematic rotation axis, like in case of grain 15 (Fig. 2B) which <c> is oriented at 45° to it, crystal lattice develops two orthogonal misorientation axes in order to accommodate the strain (Figs. 4; 5, case ii).

Selective plastic deformation of zircon grains that are aligned within XY plane (Fig. 4) could be explained with the critical resolver shear stress (CRSS) that is more easily reached along the specific planes, if their orientation is favorable (Hobbs, 1985). The preferable slip along [100] or [001] planes in zircon crystallographic structure is facilitated by the specific crystallographic orientation with respect to a local stress field.

Geometric regularities derived from the observations of natural samples

In the conditions of the simple-shear, kinematic rotation axis is assumed to be orthogonal to X-Z plane of the sample, parallel to foliation plane and normal to lineation direction (Reddy and Buchan, 2005). Schematic sketch revealing the character or zircon deformation in a shear zone is presented in Fig. 5.

The following regularities can be derived from the presented zircons deformed in a simple shear, regardless of their crystal shape and aspect ratio:

a. Zircon crystals are only plastically-deformed if their <c> aligned in the XY (foliation) plane (Fig. 4, solid circles). Zircon crystals with c-axis oblique to the XY (foliation) plane (>15□) either not deformed or fractured (Fig. 4, open circles).

b. Zircon crystals aligned to XY with <c> parallel or normal to X (stretching lineation), i.e. normal or parallel to the kinematic rotation axis, mostly develop misorientation and rotation axes [001] (Fig. 4, grains 03, 04, 24, and closely oriented).

c. Zircon crystals with <c> aligned in XY at 45° to X develop two misorientation axes (Fig. 4), which in case of grain 15 are [100] and [001].

d. Strain in plastically-deformed zircons is accommodated by formation of a continues network of low-angle boundaries, which are the result of combination of tilt and twist dislocations with <100>{010}, <100>{001}, <-110>{110}, etc. slip geometry.

The reconstruction of the kinematic rotation axis of a deformation event that formed a shear zone is important for understanding the tectonic evolution of geological units in the Earth’s crust. Based on natural data we have demonstrated a strong kinematic control on the geometry of the dominant slip systems in deformed zircon minerals.

Using the derived regularities (a)-(c) it is possible to make the reconstruction of a macroscopic tectonic frame that was causing zircon crystal-plastic deformation, and vice versa, the crystallographic orientation of zircon grain within. This gives an opportunity to attribute crystal-plastic deformation of zircon to a specific metamorphic/deformation event and thus, possibly, to derive the timing and *P-T* conditions of the latter, even for the detrital and inherited grains. Because different lattice distortion patterns in zircon are usually restricted to a specific stress-strain conditions (e.g. Kovaleva et al., 2014), therefore, they may represent a certain snapshot of the potentially complex deformation history. For example, lattice distortion pattern in analyzed grains (interconnected network of low-angle boundaries that separate strain-free subgrains) is attributed to an upper-greenschist to amphibolite facies of metamorphism. Thus, using these patterns, we can judge about the peak metamorphic conditions of the respective shear zone. The fact that some of zircon crystals indicate crystal preferred orientation points to the rigid body rotation *prior* crystal-plastic deformation, which reflects some earlier stages of rock-forming/deformation process.

Implications for zircon geochronology and further research trends

Our observations have important implications for zircon geochronology. It has been shown by a number of authors that crystal-plastic deformation can dramatically affect the content of trace elements in the domains of subjected zircon lattice and, therefore, can cause isotopic system resetting (e.g. Flowers et al., 2010; MacDonald el al., 2013; Moser et al., 2009, 2011; Piazolo et al., 2012; Reddy et al., 2006, 2007, 2009; Reddy and Timms, 2010; Timms and Reddy, 2009; Timms et al., 2011, 2012). With the help of plastically-deformed zircon it is possible to resolve the ages of such deformation events as shearing, seismic activity and meteorite impacts in terrestrial and even lunar rocks (e.g. Austrheim and Corfu, 2009; Moser et al., 2009, 2011; Nemchin et al., 2009). Based on our study, we suggest the following criteria of sample selection for the zircon mineral dating. In accordance with our regularity (a), crystals, aligned with the foliation plane of a shear zone are likely to be plastically-deformed, and thus might be (partially)rejuvenated; crystals that are at a high angle to foliation plane are unlikely to be deformed, and thus are not rejuvenated and preserve older ages. These crystal-orientation systematics potentially allow determining the age of the deformation event using in situ dating of zircons that are aligned in the foliation plane. On the other hand, if the goal is the mineral isotopic dating of the undistorted age (e.g. age of zircon crystallization), one should strictly avoid zircon grains that are aligned in the foliation plane, in order to exclude any possible age disturbances. The detailed and careful isotopic study in order to test this speculative suggestion is still waiting for its time.

Acknowledgements

This study was funded by the University of Vienna (doctoral school "DOGMA", project IK 052) and the Austrian Science Foundation Fund (FWF): I471-N19, which is part of the DFG-FWF funded international research group FOR741-DACH.

References

Austrheim, H. and Corfu, F., 2009. Formation of planar deformation features (PDFs) in zircon during coseismic faulting and an evaluation of potential effects on U–Pb systematics. Chemical Geology, 261, 25–31.

Bachmann, F., Hielscher, R., and Schaeben, H., 2010, Texture Analysis with MTEX – Free and Open Source Software Toolbox. Solid State Phenomena, 160, 63-68.

Bachmann, F., Hielscher, R., and Schaeben, H., 2011, Grain detection from 2d and 3d EBSD data-specification of the MTEX algorithm. Ultramicroscopy, 111, 1720-1733.

Bestmann, M. and Prior, D.J., 2002. Intragranular dynamic recrystallization in naturally deformed calcite marble: diffusion accommodated grain boundary sliding as a result of subgrain rotation recrystallization. Journal of Structural Geology, 25, 1597–1613.

Finch, R.J. and Hanchar, J.M., 2003. Structure and Chemistry of Zircon and Zircon-Group Minerals. In: Hanchar, J. M., Hoskin, P. W. O., eds. Zircon. Mineralogical Society of America and Geochemical Society, Reviews in Mineralogy and Geochemistry, 53, 1-26.

Flowers, R.M., Schmitt, A.K., Grove, M., 2010. Decoupling of U–Pb dates from chemical and crystallographic domains in granulite facies zircon. Chemical Geology, 270, 20–30.

Grange, M.L., Pidgeon, R.T., Nemchin, A.A., Timms, N.E., Meyer, C., 2013. Interpreting U–Pb data from primary and secondary features in lunar zircon. Geochimica et Cosmochimica Acta, 101, 112–132.

Hobbs, B.E., 1985. The geological significance of microfabric analysis, in: Preferred orientation in deformed metal and rocks. An introduction to modern texture analysis. Eds. Wenk, H. R., Elsevier Inc., 463–484.

Jeffrey, G.B., 1922. The motion of ellipsoidal particles immersed in a viscous fluid. Proceedings of the Royal Society of London, 102, 161–179, doi:10.1098/rspa.1922.0078

Kaczmarek, M.A., Reddy, S.M., Timms, N.E. 2011. Evolution of zircon deformation mechanisms in a shear zone (Lanzo massif, Western-Alps). Lithos, 127, 414-426.

Kenkmann, T., 2000. Processes controlling the shrinkage of porphyroclasts in gabbroic shear zones. Journal of Structural Geology, 22, 471-487.

Kovaleva, E., Klötzli, U., Habler, G., Libowitzky, E., 2014. Finite lattice distortion patterns in plastically deformed zircon grains. Solid Earth, 6, 1799-1861, doi: 10.5194/sed-6-1799-2014

Kovaleva, E., Klötzli, U., Habler, G., Wheeler J., 2015. Planar microstructures in zircon from paleo-seismic zones. American Mineralogist, 100, 1834-1847.

Leroux, H., Reimold, W.U., Koeberl, C., Hornemann, U., Doukhan, J.C., 1999. Experimental shock deformation in zircon: a transmission electron microscopic study. Earth and Planetary Science Letters, 169, 291–301.

MacDonald, J.M., Wheeler, J., Harley, S.L., Mariani, E., Goodenough, K.M., Crowley, Q., Tatham, D., 2013. Lattice distortion in a zircon population and its effects on trace element mobility and U–Th–Pb isotope systematics: examples from the Lewisian Gneiss Complex, northwest Scotland. Contributions to Mineralogy and Petrology, 166, 21–41.

Mainprice, D., Hielscher, R., and Schaeben, H., 2011, Calculating anisotropic physical properties from texture data using the MTEX open source package, in Prior, D.J., Rutter, E.H., and Tatham, D. J., eds, Deformation Mechanisms, Rheology and Tectonics: Microstructures, Mechanics and Anisotropy: Geological Society, London, Special Publications, v. 360, p. 175-192.

Mancktelow, N.S., Arbaret, L., Pennacchioni, G., 2002. Experimenatl observations on the effect of interface slip on rotation and stabilisation of rigid partciles in simple shear and a comparison with natural mylonites. Journal of Structural Geology, 24, 567–585.

Menegon, L., Nasipuri, P., Stünitz, H., Behrens, H., Ravna, E., 2011. Dry and strong quartz during deformation of the lower crust in the presence of melt. Journal of Geophysical Research: Solid Earth, 116, B10, doi: 10.1029/2011JB008371

Miller, C., Konzett, J., Tiepolo, M., Armstrong, R.A., Thöni, M., 2007. Jadeite-gneiss from the eclogite zone, Tauern Window, Eastern Alps, Austria: metamorphic, geochemical and zircon record of a sedimentary protholith. Lithos, 93, 68-88.

Moser, D.E., Davis, W.J., Reddy, S.M., Flemming, R.L., Hart, R.J., 2009. Zircon U–Pb strain chronometry reveals deep impact-triggered flow. Earth and Planetary Science Letters, 277, 73–79.

Moser, D. E., Cupelli, C.L., Barker, I.R., Flowers, R.M., Bowman, J.R., Wooden, J., Hart, J.R., 2011. New zircon shock phenomena and their use for dating and reconstruction of large impact structures revealed by electron nanobeam (EBSD, CL, EDS) and isotopic U–Pb and (U–Th)/He analysis of the Vredefort dome. Canadian Journal of Earth Sciences, 48, 117–139.

Nemchin, A., Timms, N. E., Pidgeon, R., Geisler, T., Reddy, S. M., Meyer, C., 2009. Timing of crystallization of the lunar magma ocean constrained by the oldest zircon. Nature Geoscience, 2, 133-136.

Pennacchioni, G. and Mancktelow, N.S., 2007. Nucleation and initial growth of a shear zone network within compositionally and structurally heterogeneous granitoids under amphibolite facies conditions. Journal of Structural Geology, 29, 1757-1780.

Piazolo, S. and Jaconelli, P., 2013. Sillimanite deformation mechanisms within a Grt-Sil-Bt gneiss: effect of pre-deformation grain orientations and characteristics on mechanism, slip-system activation and rheology. In: Deformation Structures and Processes within the Continental Crust, Eds. Llana-Fúnez, S., Marcos, A., Bastida, F. Geological Society, London, Special Publications, 394, http://dx.doi.org/10.1144/SP394.10

Piazolo, S., Austrheim, H., Whitehouse, M., 2012. Brittle-ductile microfabrics in naturally deformed zircon: Deformation mechanisms and consequences for U-Pb dating. American Mineralogist, 97, 1544–156.

Prior, D.J., 1999. Problems in determining the orientation of crystal misorientation axes for small angular misorientations, using electron backscatter diffraction in the SEM, Journal of Microscopy, 195, 217-225.

Reddy, S.M. and Buchan, C., 2005. Constraining kinematic rotation axes in high-strain zones: a potential microstructural method? In: Gapais, D., Brun, J.P., Cobbold, P.R. (Eds.), Deformation mechanisms, rheology and tectonics: from mineral to the lithosphere, 243. Special Publications. Geological Society, London, pp. 1–10.

Reddy, S.M. and Timms, N.E., 2010. Deformation of zircon and implications for geochemistry and geochronology. Source Abstracts with Programs - Geological Society of America 42, 634.

Reddy, S.M., Timms, N.E., Trimby, P., Kinny, P.D., Buchan C., Blake K., 2006. Crystal-plastic deformation of zircon: a defect in the assumption of chemical robustness. Geology, 34, 257-260.

Reddy, S.M., Timms, N.E., Pantleon, W., Trimby, P., 2007. Quantitative characterization of plastic deformation of zircon and geological implications. Contributions to Mineralogy and Petrology, 153, 625–645.

Reddy, S.M., Timms, N.E., Hamilton, P.J., Smyth, H.R., 2009. Deformation-related microstructures in magmatic zircon and implications for diffusion. Contributions to Mineralogy and Petrology, 157, 231–244.

Robinson, K., Gibbs, G. V., Ribbe, P. H., 1971. The structure of zircon: a comparison with garnet. American Mineralogist, 56, 782-790.

Selverstone, J., Morteani, G., Staude, J.-M., 1991. Fluid channelling during ductile shearing: transformation of granodiorite into aluminous schist in the Tauern Window, Eastern Alps. Journal of Metamorphic Geology, 9, 419–431.

Timms, N.E. and Reddy, S.M., 2009. Response of cathodoluminescence to crystal-plastic deformation in zircon. Chemical Geology, 261, 11–23.

Timms, N.E., Kinny, P., Reddy, S.M., 2006. Enhanced diffusion of uranium and thorium linked to crystal plasticity in zircon. Geochemical Transactions, 7, 10.

Timms, N.E., Kinny, P., Reddy, S.M., Evans K., Clark C., Healy D., 2011. Relationship among titanium, rare earth elements, U–Pb ages and deformation microstructures in zircon: Implications for Ti-in-zircon thermometry. Chemical Geology, 280, 33–46.

Timms, N.E., Reddy, S.M., Healy, D., Nemchin, A.A., Grange, M.L., Pidgeon, R.T., Hart, R., 2012. Resolution of impact-related microstructures in lunar zircon: a shock-deformation mechanism map. Meteoritics & Planetary Science, 47, 120–141.

Veselá, P., Söllner, F., Finger, F., Gerdes, A., 2011. Magmato-sedimentary Carboniferous to Jurassic evolution of the western Tauern window, Eastern Alps (constraints from U-Pb zircon dating and geochemistry). International Journal of Earth Sciences, 100, 993–1027.

Wheeler, J., Mariani, E., Piazolo, S., Prior, D. J., Trimby, P., Drury, M. R. 2009. The Weighted Burgers Vector: a new quantity for constraining dislocation densities and types using Electron Backscatter Diffraction on 2D sections through crystalline materials. Journal of Microscopy, 233, 482-494.

Wheeler, J., Mariani, E., Piazolo, S., Prior, D. J., Trimby, P., Drury, M. R. 2012. The Weighted Burgers Vector: a quantity for constraining dislocation densities and types using Electron Backscatter Diffraction on 2D sections through crystalline materials. Materials Science Forum, 715-716, 732-736.

Figure captions

Figure 1. A. Field photograph of the sampled outcrop: sample of the meta-lamprophyric dyke hosted by granitic gneiss and adjacent to the deformed aplitic dyke, highly deformed and strained. B. Thin section photographs, foliation, compositional layering and folds are clearly visible. Numbers indicate positions of the in-situ studied zircon grains, presented in this paper.

Figure 2. Deformed zircon crystals: microstructural data. Left column: cumulative EBSD maps, misorientation of every pixel is shown with respect to the user-selected reference point, marked as a white star; middle column: misorientation axes distribution plots, numbers are crystallographic directions; right column: pole figures with lower hemisphere projections of zircon crystallographic directions, color coded as corresponding EBSD map, labels indicate main crystallographic axes, black lines are reconstruction of the subgrain boundary planes. Foliation plane in figures is subhorizontal, stretching lineation is oriented at about 45° to the image plane (see description in the text). Direction of the lineation is highlighted by a red circle.

Figure 3. A. Local misorientation map of the deformed grain 04, with the superimposed Weighed Burgers Vector (WBV) components for the highlighted rectangular subareas. Gray rectangles show the areas with WBV that is comparatively low. Dotted and dashed rectangles show areas with WBV dominated by *a* or *b* components accordingly, black rectangles show areas with WBV with mixed components. In the lower right inset distribution of the misorientation axes for grain 04 is shown. B. Reconstruction of the low-angle boundaries and slip systems of the grain 04. Thick lines outside the circle indicate the direction of the low angle boundary traces; solid lines – reconstruction of low angle boundary planes; dashed lines – reconstruction of slip plane for the low-angle boundaries pointed in A. In black are the elements that correspond to the low angle boundary 1 (“LAB-1”), in gray – to low angle boundary 2 (“LAB-2”). Small circle highlights rotation and misorientation axis.

Figure 4. The pole figure with <c> (c-axis) positions of analyzed zircon grains from the studied sample. Labels in angle brackets indicate misorientation axes for the corresponding grains. Gray dashed line shows direction of foliation, gray dashed circle shows direction of lineation. Solid black circles correspond to <c> directions of grains that are plastically-deformed, empty

circles – to undeformed or fractured zircon grains. From the pole figure is clear that the <c> of all plastically deformed grains are roughly aligned with the foliation plane.

Figure 5. Schematic sketch showing zircon deformation evolution that strongly depends on its orientation in the macroscopic kinematic frame. Cases (i), (ii) and (iii) indicate plastic deformation; (i) <c> is parallel to the macroscopic kinematic rotation axis, misorientation axis is parallel to [001]. (ii): grain with <c> at an angle 45° to the kinematic rotation axis develops two rotation axes, ideally [001] and [100]. (iii) <c> is normal to the kinematic rotation axis, rotation axis is parallel to [001]. (iv) – grains with c-axes at a high angle to the foliation develop fractures or are not deformed.

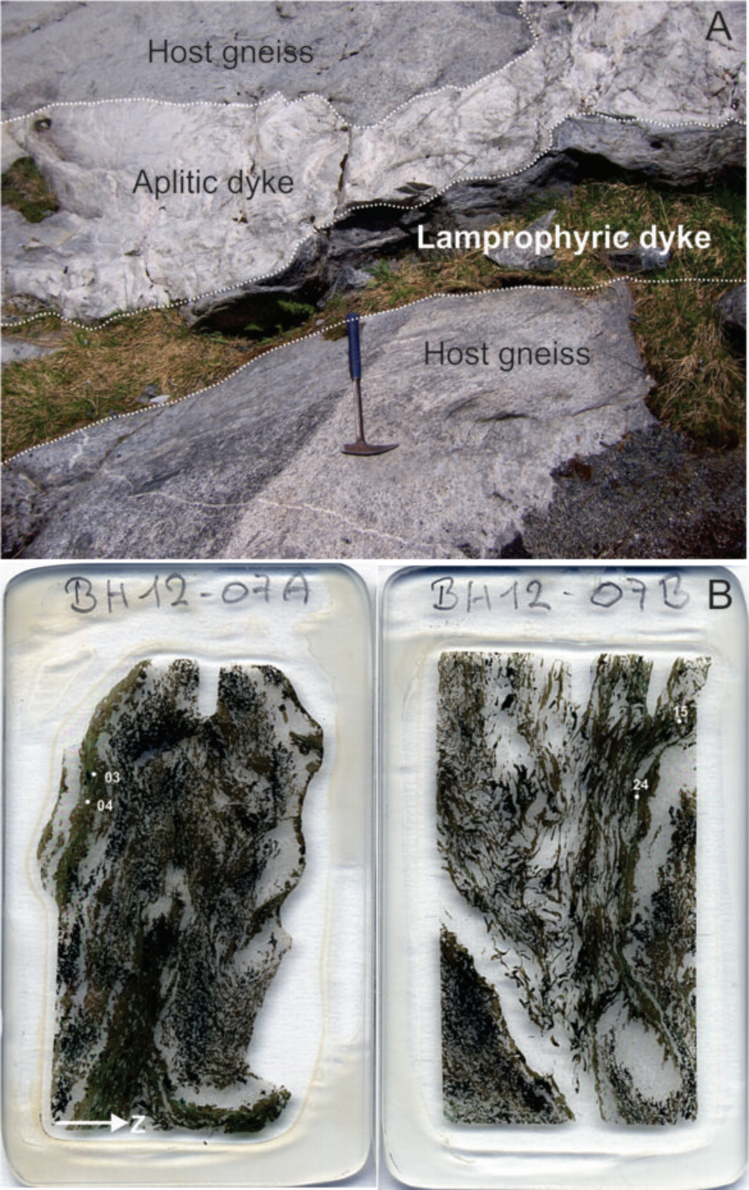
A
Host gneiss
Aplitic dyke
Lamprophyric dyke
Host gneiss
BH12-07A
BH12-07B
B
03
04
15
24
Z

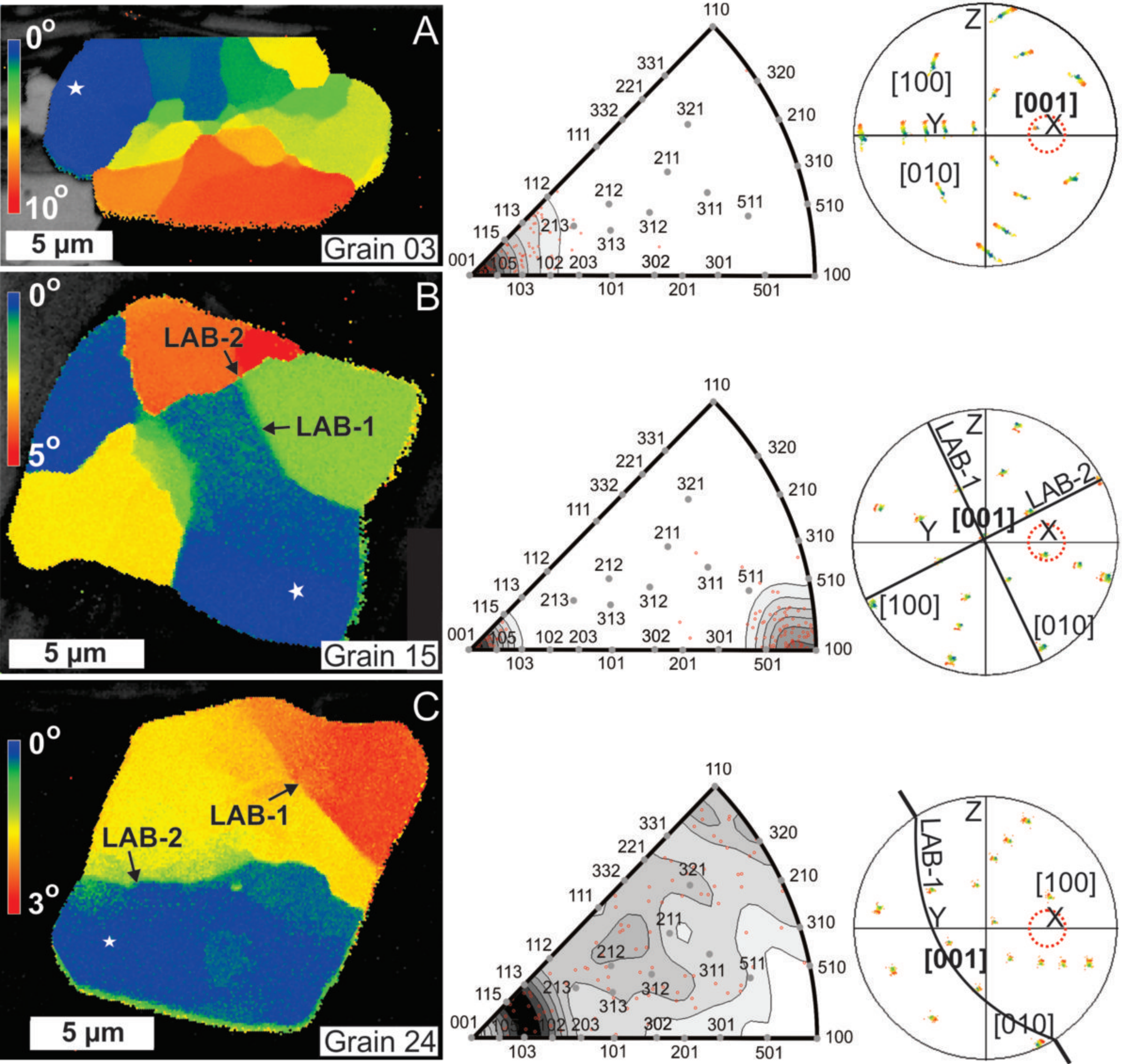
A
0°
10°
5 µm
Grain 03
110
331
221
332
111
112
113
115
001
105
103
102
203
101
302
201
301
501
100
510
310
210
320
321
211
212
213
313
312
311
511
Z
[100]
[001]
Y
X
[010]
B
0°
5°
LAB-2
LAB-1
5 µm
Grain 15
[001]
[100]
[010]
C
0°
3°
LAB-1
LAB-2
5 µm
Grain 24
[100]
[001]
[010]

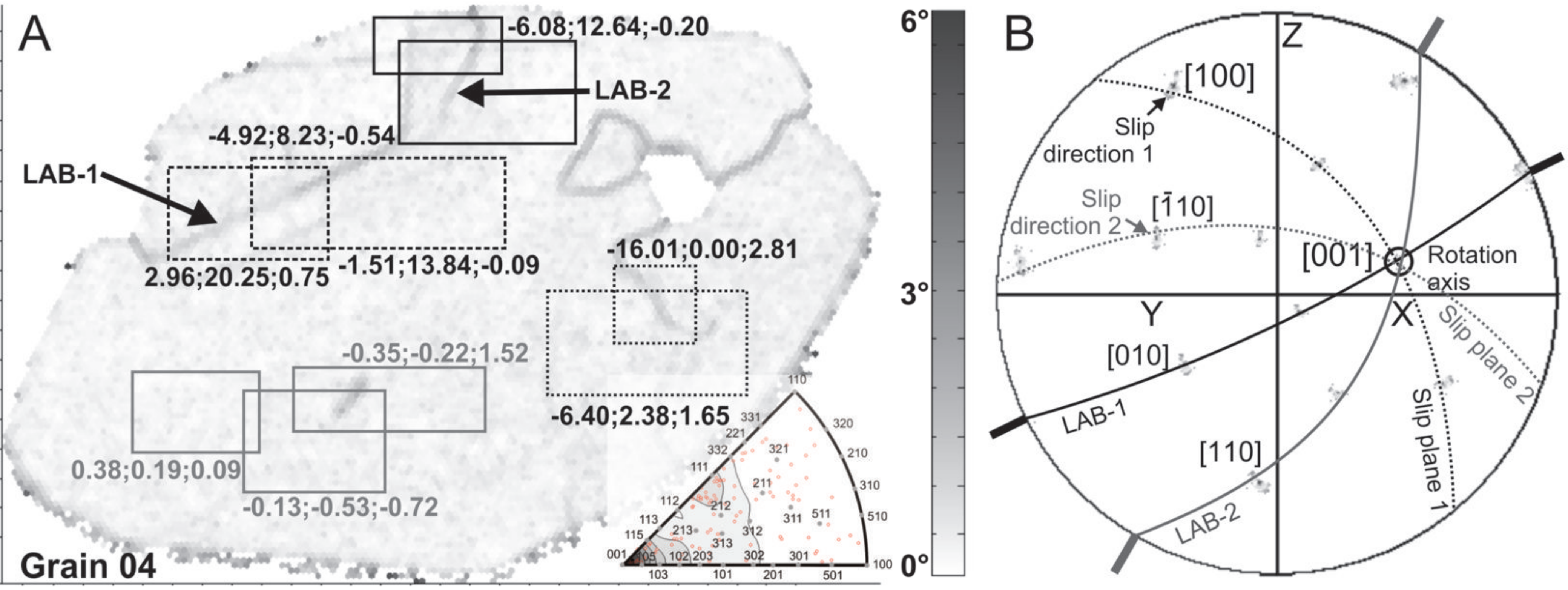
A
-6.08;12.64;-0.20
LAB-2
-4.92;8.23;-0.54
LAB-1
2.96;20.25;0.75
-1.51;13.84;-0.09
-16.01;0.00;2.81
-0.35;-0.22;1.52
-6.40;2.38;1.65
0.38;0.19;0.09
-0.13;-0.53;-0.72
Grain 04
110
331
320
221
332
321
210
111
211
310
112
212
511
510
113
311
115
213
312
313
001
105
102
203
302
301
100
103
101
201
501
6°
3°
0°
B
Z
[100]
Slip direction 1
Slip direction 2
[1̄10]
[001]
Rotation axis
Y
X
Slip plane 2
[010]
LAB-1
[110]
Slip plane 1
LAB-2

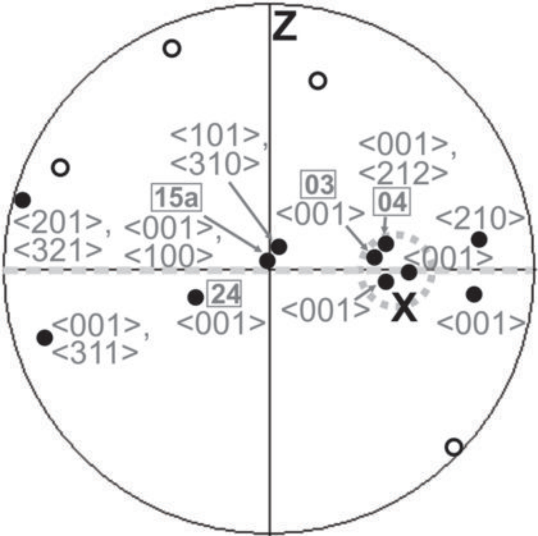
Z
<101>,
<310>
<001>,
<212>
03
15a
04
<201>,
<321>
<001>,
<100>
<001>
<210>
<001>
24
<001>
<001>
X
<001>
<001>,
<311>

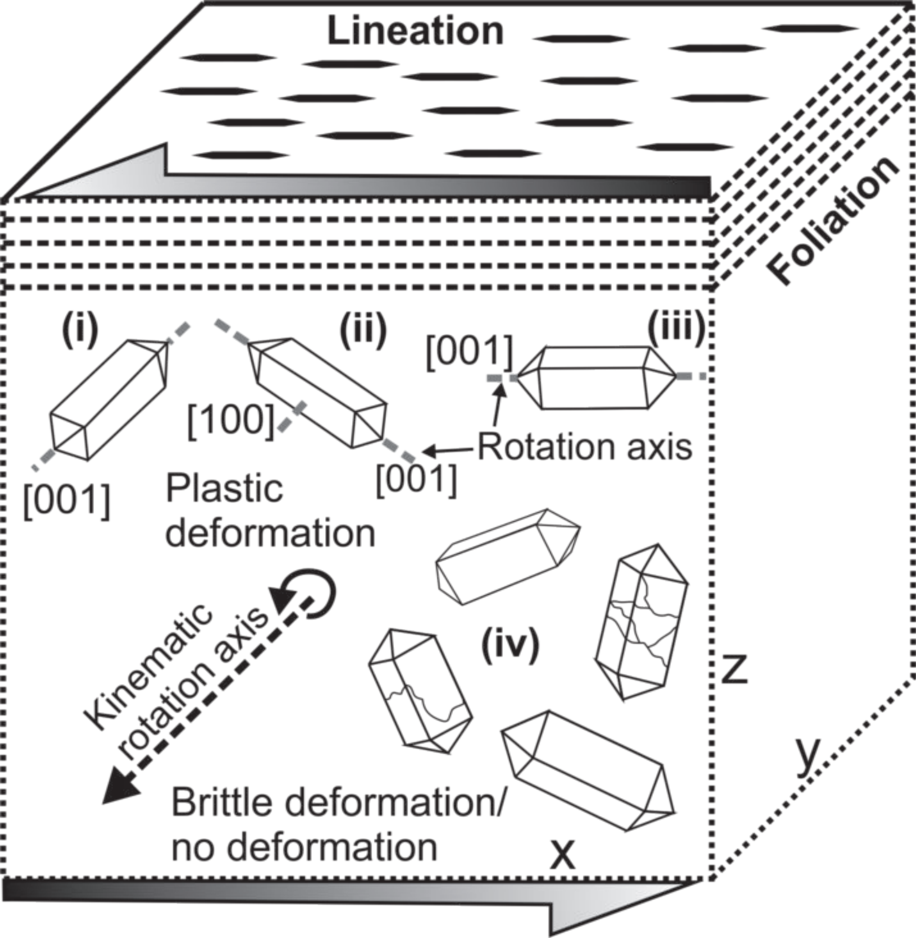
Lineation
Foliation
(i)
(ii)
(iii)
[001]
[100]
[001]
[001]
Rotation axis
Plastic deformation
Kinematic rotation axis
(iv)
z
y
x
Brittle deformation/ no deformation